Stimuli-responsive nanoparticle-nanofiber hybrids for drug delivery and photodynamic therapy

Gözde Kabay [a,b,1,*], Ahmet Ersin Meydan [a,c,1], Taesik Eom [d], Bong Sup Shim [d], Mehmet Mutlu [a,e], Gizem Kaleli-Can [a,f,*]

[a] Plasma Aided Biomedical Research Group (pabmed), Department of Biomedical Engineering, TOBB University of Economics and Technology, 06560 Ankara, Turkey
[b] Karlsruhe Institute of Technology, Institute of Functional Interfaces – IFG, 76344 Karlsruhe, Germany
[c] Department of Molecular Medicine, Graduate School of Health Sciences, TOBB University of Economics and Technology, 06560 Ankara, Turkey
[d] Soft Matter Laboratory, Department of Chemical Engineering, Inha University, Incheon 402-751, South Korea
[e] Department of Material Science and Engineering, Faculty of Engineering, Ostim Technical University, 06374 Ankara, Turkey
[f] Department of Biomedical Engineering, İzmir Democracy University, 35140 İzmir, Turkey

ARTICLE INFO

Keywords:
Melanoma
Eumelanin
Electrospinning
Zero-order kinetics
Photodynamic therapy

ABSTRACT

Hybrid nanomaterials possess integrated multi-components to syncretize various properties and functions within a single entity. Owing to this synergistic effect, they promise efficient anti-cancer therapy. In line with this target, we produced stimuli-responsive nanoparticle-nanofiber hybrids (NNHs) via embedding photoresponsive natural melanin nanoparticles (MNPs) within a biocompatible polycaprolactone (PCL) nanofiber matrix. Electrospinning was performed to produce monolithic and core–shell structured NNHs using a single and a coaxial nozzle. The NNHs were upgraded to drug delivery systems by model hydrophilic drug-ampicillin (amp)-loading. The drug release results showed that monolithic PCL meshes displayed a burst release, whereas nanohybrid formation with MNPs improved the release profile toward Fickian diffusion. Core-shell NNH presented a more sustained drug release profile than its MNP-free replica and monolithic NNH because its encapsulating shell layer hindered the diffusion of the drug. The photodynamic therapy accompanied by UV-A-irradiation on monolithic and core–shell NNHs yielded up to 34 % and 37 % malignant melanoma cell death. Moreover, this study proved the potency of MNPs-enhanced NNHs in drug delivery and photodynamic therapy applications. Even so, more efforts should be concerted to unlock unknown features of the NNHs, which have the power to advance emerging areas, including but not limited to material science, biosensing, and theranostics.

1. Introduction

Since Feynman influenced several researchers to look into the matter differently (Feynman, 1992), explorations in the material science field have been progressively boosted. Notably, particular interest has been given to nanomaterials research. Thus far, many nanomaterials have been synthesized from several origins (e.g., organic, inorganic, and hybrids) in diverse forms (e.g., nanoparticle, nanofiber, nanowires, and quantum dots), which have been utilized in various domains, particularly for biomedical applications, energy storage, and electronics. Currently, due to the urge to control the spread of the COVID-19 pandemic (Kabay et al., 2022), pharmaceutical applications of nanomaterials are spotlighted, and current efforts are shifted toward nanoparticle (NP) research, particularly for vaccine development. In this context, lipid-NPs carrying short-lived strands of genetic material, namely messenger ribonucleic acid (mRNA) shielded with polyethylene glycol (PEG), have established success in vaccine delivery (Buschmann et al., 2021; Sahin et al., 2021; Schoenmaker et al., 2021). When NPs utilized as a pharmaceutical nanocarrier, they offer many advantages; however, several inquiries regarding their safety (Anand and Stahel, 2021), efficacy (Baden et al., 2021; Polack et al., 2020), cytotoxicity (Anand and Stahel, 2021), and stability (Schoenmaker et al., 2021) exist.

To bypass the drawbacks mentioned above, NPs integration within/onto biocompatible, biodegradable, excretable, and chemically stable

* Corresponding authors at: Karlsruhe Institute of Technology, Institute of Functional Interfaces – IFG, 76344 Karlsruhe, Germany (G. Kabay). İzmir Democracy University, 35140 İzmir, Turkey (G. Kaleli-Can).
E-mail addresses: gozde.kabay@kit.edu (G. Kabay), gizem.kalelican@idu.edu.tr (G. Kaleli-Can).
[1] These authors contributed equally to this work.

matrices in the form of films (Bryaskova et al., 2010), fibrous meshes (Adhikari et al., 2019), hydrogels (Clasky et al., 2021; Loh et al., 2010; Nakielski et al., 2020), and 3-D printed materials (Tang et al., 2021) have been explored. In this direction, several ex-situ or in-situ techniques, such as self-assembly, phase separation, template- or pattern-assisted growth, and hydrothermal synthesis pathways, have been surveyed (Qiao et al., 2018). Among these, the electrospinning method steps forward due to offering a versatile approach for generating nanoparticle-nanofiber hybrids (NNHs) and enabling low-cost mass production. Such electrospun NNH platforms are exploited in a wide range of application areas, including energy (Liu et al., 2020; Pan et al., 2017), tissue engineering (Ma et al., 2021; Morsink et al., 2022), wound healing (Dong and Guo, 2021), and particularly drug delivery applications (Bohara, 2019; Taylor-Pashow et al., 2010; Wang et al., 2010).

The electrospinning method also enables the versatile production of stimuli-responsive NNHs that can compensate for the disadvantages of conventional dosage forms (Katz and Willner, 2004; Taylor-Pashow et al., 2010) and nanoparticle-drug formulations (Ajdary et al., 2018; Jeevanandam et al., 2018; Katz and Willner, 2004). Still, only a few studies explored stimuli-responsive NNH platforms for such use. For example, magneto- and opto-stimuli triggered rhodamine B release (Banerjee et al., 2021) was achieved with the superparamagnetic iron oxide NPs (SPIONs) and polycaprolactone (PCL) based hybrid system. After applying an external magnetic force and laser illumination, the Néel relaxation of heat-generating SPIONs elevated structural changes on the thermosensitive PCL nanocarrier. Adjustment of external stimulation enabled control of the SPIONs entrapped drug release rate from its encapsulating matrix. Another study (Nakielski et al., 2020) explored thermoresponsive hydrogels made of poly(*N*-isopropyl acrylamide) in combination with gold nanorods. They built a stimuli-responsive plasmonically-enhanced hydrogel nanocomposite that was later entrapped by a poly(L-lactide) nanocarrier consisting of Rhodamine B. The localized temperature rises, and the water expulsion from a nanostructured hydrogel enabled on-demand delivery of Rhodamine B. The synergic hybrid combination promises simultaneous therapy, for instance, anticancer therapy and antibacterial treatment. Although examples can be varied, most NNHs were produced by carbon, metal, and metal-oxide-based NPs embedding within a polymeric carrier matrix. However, to our knowledge, no investigation on auspicious natural material, eumelanin, has been carried out to build a stimuli-responsive NNH platform.

Melanin is a dark pigment in living organisms that can be found in five different structural forms: eumelanin, pheomelanin, allomelanin, pyomelanin, and neuromelanin (Eom et al., 2016). Eumelanin extracted from natural resources mainly consists of 5,6-dihydroxyindole (DHI), 5,6-dihydroxyindole-2-carboxylic acid (DHICA), and their oxidized forms having molecular functional groups: catechol, amine, and imine. It offers several advantages, such as electrical conductivity (Eom et al., 2017), adaptability for chelating with metal ions (Kaleli-Can et al., 2020), optical- and magnetic-stimuli triggering (Brenner and Hearing, 2008; Chiarelli-Neto et al., 2014; Gabriele et al., 2021; Mavridi-Printezi et al., 2020; Xiao et al., 2020; Zhang et al., 2015), and radical scavenging (Felix et al., 1978a; Rozanowska et al., 1999). Likewise, its additional features include good biocompatibility and biodegradability, high drug binding affinity, intrinsic photoacoustic properties, and pH responsiveness (Araújo et al., 2014; Ozlu et al., 2019), appealing for drug delivery applications. Through entrapping melanin nanoparticles (MNPs) within a biocompatible polymeric matrix, such as polycaprolactone (PCL) (Endres and Siebert-Raths, 2012), the disadvantages arising from conventional dosage forms or NP formulations administration can be overcome.

In this context, we fabricated multifunctional NNHs made of melanin nanoparticles-PCL nanofiber (MNPs-PCL) and model hydrophilic drug ampicillin (amp). Single- and coaxial-nozzle electrospinning was performed to produce monolithic and core–shell structured NNHs. PCL and amp are incompatible substances due to their different polarities. Such a low-compatible component combination within a single matrix is expected to result in the loaded drugs' burst release. Previously, we showed that coaxial electrospinning could disregard this burst release effect (Sultanova et al., 2016). With this study, we expanded the frame of our previous work by examining the impact of MNP-mediated nanohybrid formation on the release behavior of amp. The hybrid NNHs showed controlled and sustained release of the model drug from single-and core–shell NNHs. In addition, photodynamic therapy of malign melanoma cells was achieved by stimulating the NNHs with UV-A light. The photoactivation of natural photosensitizer MNPs within the NNHs could effectively inhibit malignant melanoma cell expression. Overall, the results of this study suggest that the offered NNHs can be efficiently exploited as a transdermal patch for transdermal malignant melanoma therapy.

2. Materials and method

2.1. Materials

MNPs were extracted from commercial cuttlefish ink paste purchased from Chef's Food (South Korea). All experiments were carried out with ultra-pure water (UPW, 18.25 MΩcm; at 25 °C, Thermo Scientific, USA). Polycaprolactone (PCL), methanol, ampicillin sodium salt (amp), phosphate-buffered saline (PBS) tablets (pH: 7.4), and sodium azide (NaN3) were purchased from Sigma-Aldrich (USA). Chloroform was obtained from Merck (Germany).

Dulbecco's modified Eagle's medium (DMEM), Eagle's minimal essential medium (EMEM), Dulbecco's phosphate buffer saline solution (DPBS), fetal bovine serum (FBS), sodium pyruvate solution, tryptic soy agar (TSA), tryptic soy broth (TSB), and 3-(4,5-dimethylthiazol-2-yl)-2,5-diphenyltetrazolium bromide (MTT) were purchased from Sigma Aldrich (USA). Dimethyl sulfoxide (DMSO) was obtained from ISOLAB Laborgeräte GmbH (Germany). Penicillin-streptomycin solution and trypsin-EDTA solution were purchased from Biological Industries (Israel). BJ healthy human skin fibroblast cell line (ATCC® CRL-2522™), A375 human malignant melanoma cell line (ATCC® CRL-1619™), *Escherichia coli* (*E. coli*, ATCC® 25922™), and *Staphylococcus aureus* (*S. aureus*, ATCC® 25923™) were purchased from American Type Culture Collection (ATCC®, USA).

2.2. Nanoparticle production

Melanin extraction was achieved using an ink paste of commercially available *Sepia Officinalis* (cuttlefish) following a previous method (Fig. 1) (Eom et al., 2019, 2016; Liu and Simon, 2003). The MNPs were purified in five repetitive cycles containing dilution and centrifugation (3500 rpm, 10 min) of the ink paste to remove salt and other water-soluble impurities (Xie et al., 2021). After each cycle, the supernatant was removed, and the final pellet was dried at 60 °C overnight. Dry MNP powders were collected and stored in a desiccator before usage.

2.3. Production of multifunctional nanoparticle-nanofibrous hybrid meshes

So far, various technologies such as electrospinning (Wang et al., 2012; Zhang et al., 2022), template synthesis (Zhao et al., 2020), phase separation (Ji et al., 2021), and their combination (Deng et al., 2021) have been used to produce nanofibers. However, such methods require additional chemical steps to incorporate NPs with a nanofiber and/or are unsuitable for forming hybrid nanocomposites. Electrospinning is one of the most convenient techniques to prepare uniform, solvent-free NNHs in one step; therefore, it is selected as a tool for forming monolithic and core–shell structured meshes in this study.

The electrospinning setup used in this study incorporates a high voltage direct current (DC) power supply (MCH 303D2, Gamma High Voltage Research Inc., USA), syringe pumps (NE-1000, New Era Pump Systems, USA), a coaxial nozzle (Inovenso, Istanbul, Turkey) and a metal

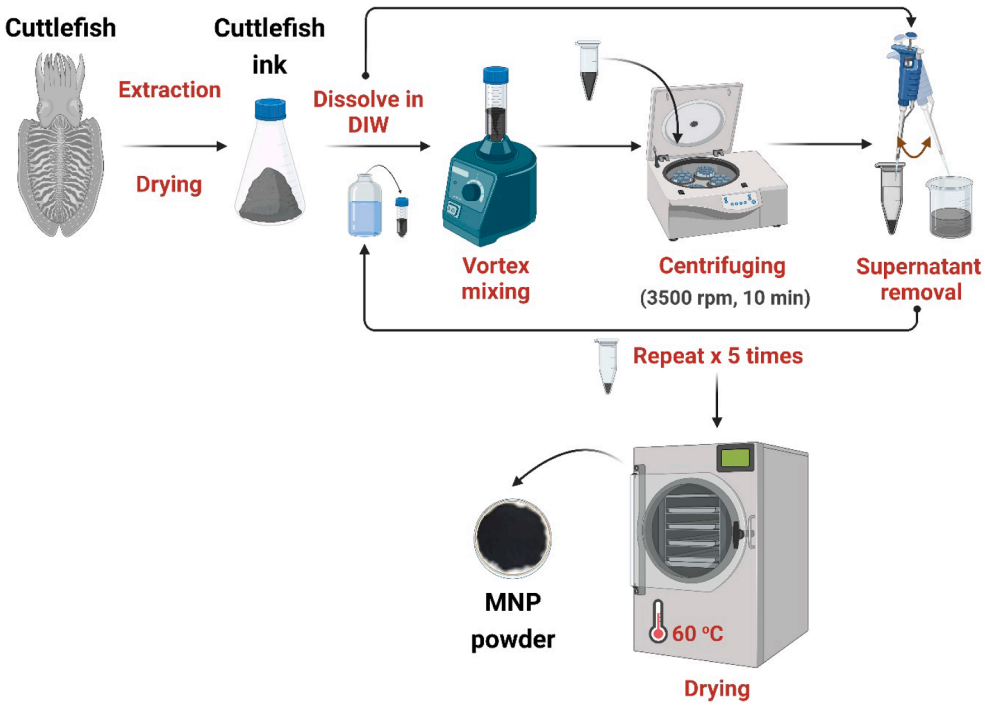

Fig. 1. Schematic illustration showing the extraction and purification steps of MNP powder. The figure was created with Biorender.com.

collector as sketched in Fig. 2. Both monolithic and core–shell (CS) meshes were produced using the same coaxial nozzle. However, only the core solution was placed in the upper syringe pump and fed to produce the monolithic fibers. For hybrid fibers production, two syringes containing core or shell solutions were separately inserted in the coaxial nozzle and were simultaneously fed.

The parameters we previously optimized for PCL electrospinning were applied for the electrospinning of NNHs (Sultanova et al., 2016). To investigate the influence of electrospinning parameters and hybrid formation on the physicochemical properties of the produced fibers, three different types of NNHs, namely monolithic NNH (CR), core–shell 1 NNH (CS1), and core–shell 2 (CS2) NNH, were produced. All electrospinning solutions used to produce NNHs and electrospinning parameters are given in Table 1.

2.4. Characterization

A particle size analyzer measured the zeta potential and hydrodynamic size distribution of MNPs (ELS-Z2 Otsuka). The morphology of the MNP powders, CR, CS1, and CS2 meshes was monitored using a scanning electron microscope (SEM; FEI-Quanta 200 FEG and Apreo S model-FEG, Thermo Scientific, USA). Before the examination, the

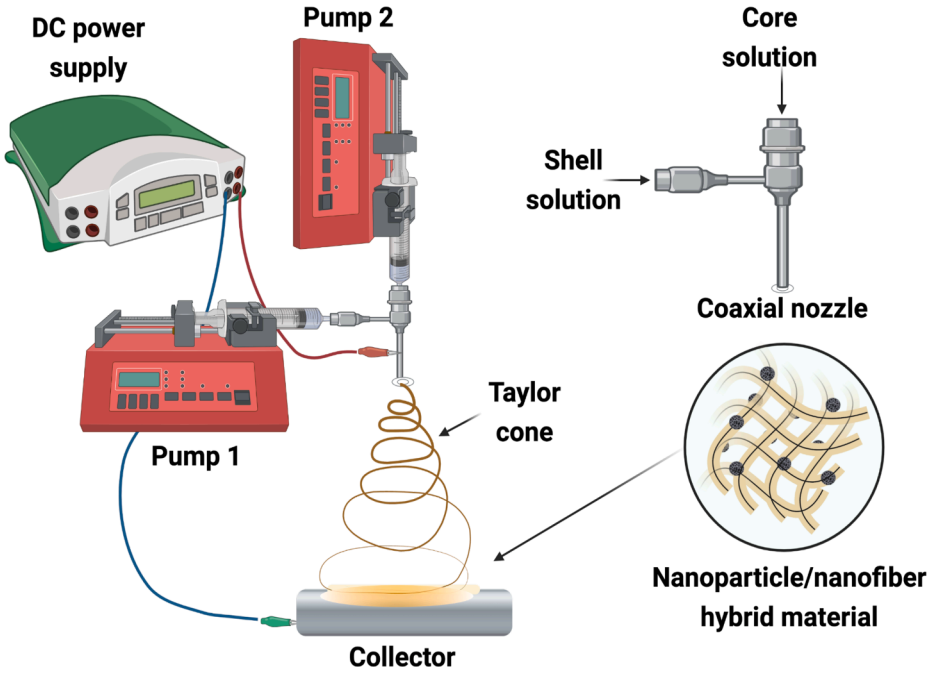

Fig. 2. The schematic representation of the horizontally placed electrospinning setup consists of two syringe pumps to feed either solely core solution (to produce CR) or core and shell solutions (to make CS1 and CS2). Once the loaded solution(s) reaches the nozzle tip, a DC voltage is applied between the nozzle tip and the collector plate to form a Taylor Cone and, consequently, (nano)fibers. Theoretically, careful optimization of the parameters associated with the solution properties (e.g., surface tension, conductivity/solution charge density, viscosity/concentration, electrospinning apparatus (e.g., tip-to-collector distance, flow rate, and voltage), and environment conditions (e.g., temperature, humidity, air velocity) allow producing continuous nanofibers with various forms and morphologies (Qiao et al., 2018). The figure was created with Biorender.com.

Table 1
Solution compositions and device parameters used to produce NNHs utilizing single- and coaxial-nozzle electrospinning. Control meshes were also produced without amp addition and used for comparison throughout the analyses. For the core solution, 10 % PCL was prepared by dissolving PCL in (9:1, v:v) chloroform: methanol mixture. Then, 1 % amp (1:10, w:w, amp:PCL) and 0.1 % MNPs (1:1000, w:w, MNP:PCL) were added to the PCL mixture. For the shell solution, 4 % PCL was prepared before adding 0.4 % MNP (1:1000, w:w, MNP:PCL). Abbreviations: CR: monolithic NNH, CS1: core–shell NNH 1, CS2: core–shell NNH 2).

Mesh type	Chemical composition of the electrospinning solutions		Flow rate (mL/h)		Distance (cm)	Voltage (kV)
	Core fluid	Shell fluid	Core solution	Shell solution		
CR	10 % PCL 1 % amp 0.1 % MNPs	–	1.0	–	9	12
CS1 CS2	10 % PCL 1 % amp	4 % PCL 0.4 % MNP	0.5	0.5 0.6		

samples were sputter-coated with a gold/palladium (Au/Pd) mixture. For better spatial resolution, the accelerating voltage and spot size were adjusted to 7.5 kV and 1–5 μm, respectively. The average size of nanoparticles and nanofibers was determined by measuring diameters from 100 randomly selected locations in SEM images using ImageJ® software (NIH, MD, USA). The core–shell NNHs were investigated using a transmission electron microscope (TEM, FEI Tecnai, G2-F30, USA) at a 200-kV accelerating voltage after placing the specimens onto a 300-mesh copper grid.

For chemical composition analyses, a Thermo K-Alpha instrument and a Thermo K-Alpha monochromatic high-performance XPS spectrometer (XPS, ThermoFisher Sci., USA) were employed at a pressure of $1x10^{-9}$ Torr. A micro-focused X-ray beam with a diameter of 400 μm was focused on a randomly selected sample portion for analysis. Spectra were recorded with an energy step width of 0.8 eV, a 187.85 eV analyzer pass energy, and an acquisition time of 160 ms per data point. Peak fitting and deconvolution were performed with OriginLab® v.6 software. The attenuated total reflectance-Fourier transform infrared (ATR-FTIR) spectroscopy analyses were conducted to examine compatibility between the components. The IR spectra of MNP, amp, PCL powders, single-nozzle electrospun monolithic meshes (amp-PCL, MNPs-PCL, and CR), and coaxially electrospun core–shell fiber mesh (CS) were collected after scanning their respected absorbance within 4000–1000 cm^{-1} wavenumber range using an IR spectrometer (Perkin Elmer Spectrum, 100, USA). The thermal characteristics of samples were analyzed via thermal gravimetric analysis (TGA, TA Instruments Co., USA) under a nitrogen atmosphere. The alterations in the initial mass of the sample pieces (2–5 mg) were screened under constant heating (10 °C/min) to evaluate decomposition profiles.

2.5. In vitro drug release

For drug release testing, electrospun meshes were cut into 1 cm × 1 cm pieces, and each piece was immersed in an amber bottle containing 0.1 M PBS (pH: 7.4, 4 mL) solution and 0.1 % NaN_3 (w:v). All samples were placed into an incubator shaker (Innova® 40R, New Brunswick™, Germany) and stirred at 50 rpm speed at 37 °C temperature for 144 h. At predetermined time points (0.25, 0.50, 0.75, 1, 2, 4, 8, 12, 24, 48, 72, 96, 120, and 144 h), 1 mL of release medium was removed and substituted with fresh PBS (pH: 7.4) solution to keep the buffer volume constant. The collected mediums were directly analyzed with a UV–vis spectrophotometer (U5100, Hitachi U-5100, Japan). Consequently, the release data obtained for each NNH were fitted to several kinetic models (zero-order, first-order, Korsmeyer-Peppas, and Higuchi models). Drug release studies were carried out in triplicates for all NNHs, and the data were reported as the mean (%) ± standard deviation (mean ± SD) of three replicate measurements. The drug release mechanism for each NNH was determined based on the highest regression coefficient (R^2) obtained.

2.6. Antibacterial testing

Antibacterial properties of MNPs and amp-free meshes, including PCL, CR, CS1, and CS2, were tested against Gram-negative *Escherichia coli (E. coli*, ATCC® 25922™) and Gram-positive *Staphylococcus aureus* (*S. aureus*, ATCC® 25923™) strains under aseptic conditions. First, lyophilized *E. coli* and *S. aureus* strains were rehydrated with tryptic soy broth and incubated (IN110, Memmert, Germany) at 37 °C for 30 min. Next, bacteria were inoculated with tryptic soy agar and passaged twice before cell seeding.

The optical densities of each bacterial suspension were adjusted to 0.5 McFarland (corresponding to 1.5×10^8 CFU/mL of bacterial concentration) using tryptic soy broth medium addition measured by densitometer (DEN-1, Biosan, Latvia). 100 μL of each bacterial suspension diluted 100-fold with TSB were transferred into 96-well plates and incubated at 37 °C for 24 h for bacterial adhesion. After removing non-attached/dead cells, varying MNP concentrations and nanofibrous meshes were separately placed onto the formed biofilms and incubated at 37 °C for 24 h. Then mediums were aspirated and washed, and 200 μL of MTT solution (0.5 mg/mL in TSB) was added before final incubation (37 °C for 3 h). For all washing steps, sterile DPBS (pH:7.4) was used. Following washing, optical densities of formed formazan crystals dissolved in DMSO (Thermo Scientific, Multiskan Go, USA) were measured at 540 nm. The calculated bacterial viabilities were reported as mean ± coefficient of variance (mean ± CV) obtained by six replicate measurements (n = 6).

In addition to the MTT test, the antibacterial effect was monitored through inhibition zone examination. The bacterial suspensions were inoculated to Columbia sheep blood agar plates and used to control for bacterial growth. Then, amp-containing (CR, CS1, and CS2) and amp-free (CR-B, CS1-B, and CS2-B) meshes were put into the center of the Petri dishes containing *E. coli* and *S. aureus* and incubated at 37 °C for 24 h (Supplementary Material, Table S1).

2.7. In vitro cytotoxicity

The in vitro cytotoxicity of the MNPs and amp-free NNHs against fibroblast cells (CRL-2522) was investigated by MTT assay. The fibroblasts were seeded and cultured in a flask using EMEM (including 10 % FBS, 1 % sodium pyruvate, 1 % L-glutamine, and 1 % penicillin–streptomycin solution). In contrast, the melanoma cells were cultivated with DMEM (high glucose supplemented with 10 % FBS, 2 % L-glutamine, and 1 % penicillin–streptomycin solution) in a humidified CO_2 atmosphere in a 37 °C incubator (Model: 371, Thermo Scientific, USA). All cultured cells were dissociated with 0.25 % trypsin-EDTA, centrifuged, and resuspended in a medium before being seeded.

Accordingly, 30×10^3 fibroblast cells were seeded in 48-well plates and incubated for 24 h to obtain a confluent monolayer formation. Following the incubation, the cells were treated with MNPs (0–200 μg/mL) (Supplementary Material, Fig. S1), CR, CS1, and CS2 meshes for 24 h at 37 °C. Afterward, the wells were washed with DPBS to remove non-attached/dead cells. Then, the MTT solution (0.5 mg/mL) was transferred into each well, and the resultant mixtures were incubated for four hours before DMSO was added. The optical density of the formazan solution was colorimetrically measured at 540 nm wavelength to

calculate the cell viability. The tissue culture plate surface (TCPS) was used as a negative control. The cell viability results were reported as the mean ± coefficient of variance (mean ± CV) obtained by six replicate measurements (n = 6).

2.8. Photodynamic therapy

Before initiating the photodynamic therapy, the melanoma cells (15 × 10^3) were seeded in a 48-well plate and incubated for 24 h for a monolayer formation. After the culture medium was aspirated, UV-sterilized MNP powders, CR, CS1, and CS2 meshes were transferred onto the cell monolayer and fixed by a cloning cylinder for optimum material-cell interaction. All samples were incubated for 24 h at 37 °C. First, the cell viability on each sample mesh was measured without any external stimulus (t = 0). Later, the optical stimulation was created by a light source (CAMAG, CH) that generates UV-A range (at 366 nm wavelength) electromagnetic radiation. After the distance between the well plate surface and the light source was adjusted to 2 cm, each sample was subjected to UV-A irradiation for 2, 5, and 10 min. Ultimately, the MTT assay (Section 2.6.2) was performed to examine the influence of photodynamic therapy on melanoma cell viability. For data normalization, TCPS was taken as NC for free-MNPs, whereas PCL mesh was used as NC for CR, CS1, and CS2, respectively. The data evaluation and their pairwise comparison were carried out using Tukey's honestly significant difference (HSD) method (* p <=0.05, *** p <=0.001). The results were reported as the normalized mean ± coefficient of variance (mean ± CV) of six replicate measurements (n = 6).

3. Results and discussions

3.1. Melanin nanoparticle production and characterization

The MNPs were analyzed in the dry state and aqueous environment to see the effect of water dispersion on their size and morphology. The SEM images showed that the freeze-dried MNPs were spherically shaped with 134.5 ± 37.3 nm diameter (Fig. 3**a-b**). The average hydrodynamic diameter and the zeta potential of the MNPs in water were found as 142.4 ± 38.7 nm and –33.7 ± 1.8 mV. These results confirm the thermodynamic stability of MNPs, which originates from the repulsion of the electrical double layer when dispersed in water (Eom et al., 2017).

XPS spectra of MNPs are given in Fig. S2 (Supplementary Material). The high-resolution C-1 s signal of MNPs was fitted with three components at 284.3 eV, 285.9 eV, and 286.2 eV, which corresponded to C—C, C—OH, and C—O, respectively. Then, N-1 s spectra were deconvoluted, and a single peak corresponding to C—NH_2 (399.6 eV) was seen. Since cuttlefish ink predominantly contains eumelanin, MNPs extracted from this source are also called eumelanin nanoparticles. In the eumelanin synthesis reaction, two precursors, 5,6-dihydroxyindole and dihydroxyindole-2-carboxylic acid, are known to be involved, also confirmed by the presence of C—C, C—OH, C—O, and C—NH_2 groups in the XPS spectra (Kaleli-Can et al., 2020).

3.2. Nanoparticle-nanofiber hybrid systems

All electrospun meshes were characterized with SEM analyses to investigate morphological variances between the monolithic and core–shell meshes (Fig. 4). The diameters of CR, CS1, and CS2 hybrid meshes were measured from their respective SEM images. The average diameter values were calculated as 672.4 ± 104.9 nm, 391.9 ± 58.9 nm, and 519.8 ± 88.2 nm for CR, CS1, and CS2. CS1 and CS2 have smaller diameters than CR because their entrapping shell layer has less PCL content (4 % wt.) than the CR mesh (10 % wt.). Although electrospinning process parameters were identical, MNP addition caused a slight increment in the average fiber diameter of monolithic NNHs than the amp-PCL mesh (Sultanova et al., 2016). Nevertheless, the Taylor cone and the fiber jet formed while producing the CS1 (0.5 mL/h) hybrid

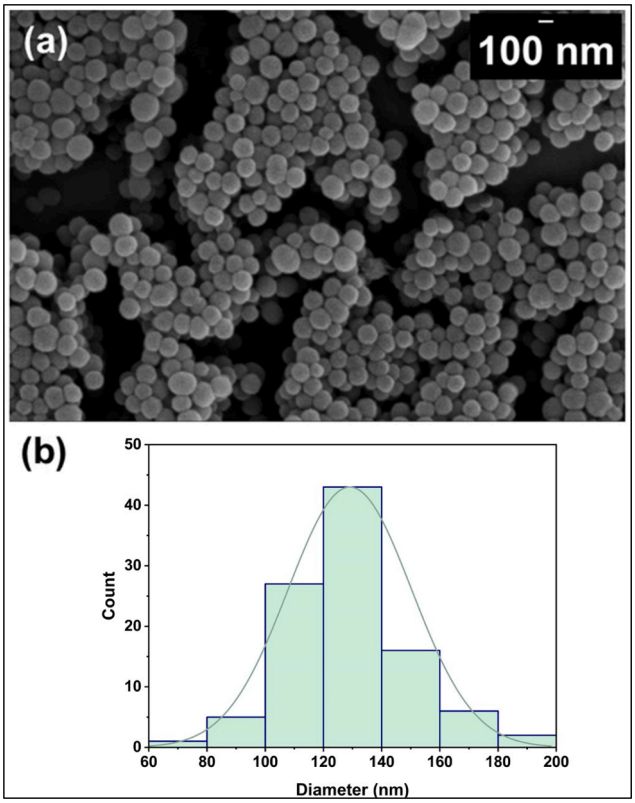

Fig. 3. SEM image of extracted and purified MNPs (a) and their diameter distribution graph (b). ImageJ® software was used to measure particle diameters. Data analyses were performed with OriginLab® software and are presented as mean ± SD (n 100).

were more stable than the ones formed while producing the CS2 hybrid. This situation can be explained by the slightly higher shell flow rate (0.6 mL/h) used for CS2 hybrids' production. Unstable jet formation resulted in variations in the mean fiber diameters, possibly due to the electrospinning of low compatible drug-polymer-particle combinations and/or tip clogging.

Moreover, TEM images of CS1 and CS2 meshes were collected to investigate the core–shell formation, and their respective thicknesses were identified (Fig. 4**d** and Fig. 4**e**). The fiber that belongs to the CS1 mesh had an inner core diameter of 260.8 nm, whereas the upper shell and lower shell thicknesses were measured as 68.4 nm and 69.5 nm, respectively. For CS2, the inner core diameter was measured at 276.6 nm, while the upper and lower shell thicknesses were 142.7 and 129.1 nm, suggesting an asymmetric core–shell formation due to the instability of the Taylor cone at the higher shell flow rate (0.6 mg/mL vs 0.5 mg/mL), or partial clogging of the nozzle tip. Nanofiber diameter distributions obtained from the SEM images of each NNH and their corresponding mean ± SD values are also given in Fig. 4**f**.

3.2.1. Drug compatibility analyses

Compatibility (defined by secondary interactions like hydrogen bonding) between drugs and matrix constituents is essential to minimize the burst release of the loaded drug (Kabay et al., 2018, 2017; Sultanova et al., 2016). Therefore, in this study, ATR-FTIR spectroscopy analyses investigated the effect of monolithic and core–shell formation on the compatibility between the amp and the NNHs' constituents. The obtained spectra are given in Fig. 5.

Briefly, the IR spectra of amp powder showed the stretching of —OH and —NH peak at 3327 cm^{-1}, —CO stretching band 1767 cm^{-1} and —NH bend of 1° amine 1604 cm^{-1}. The spectrum of PCL powder peaked at 2949 cm^{-1}, 2903 cm^{-1}, and 2871 cm^{-1} (—C—H stretching vibration

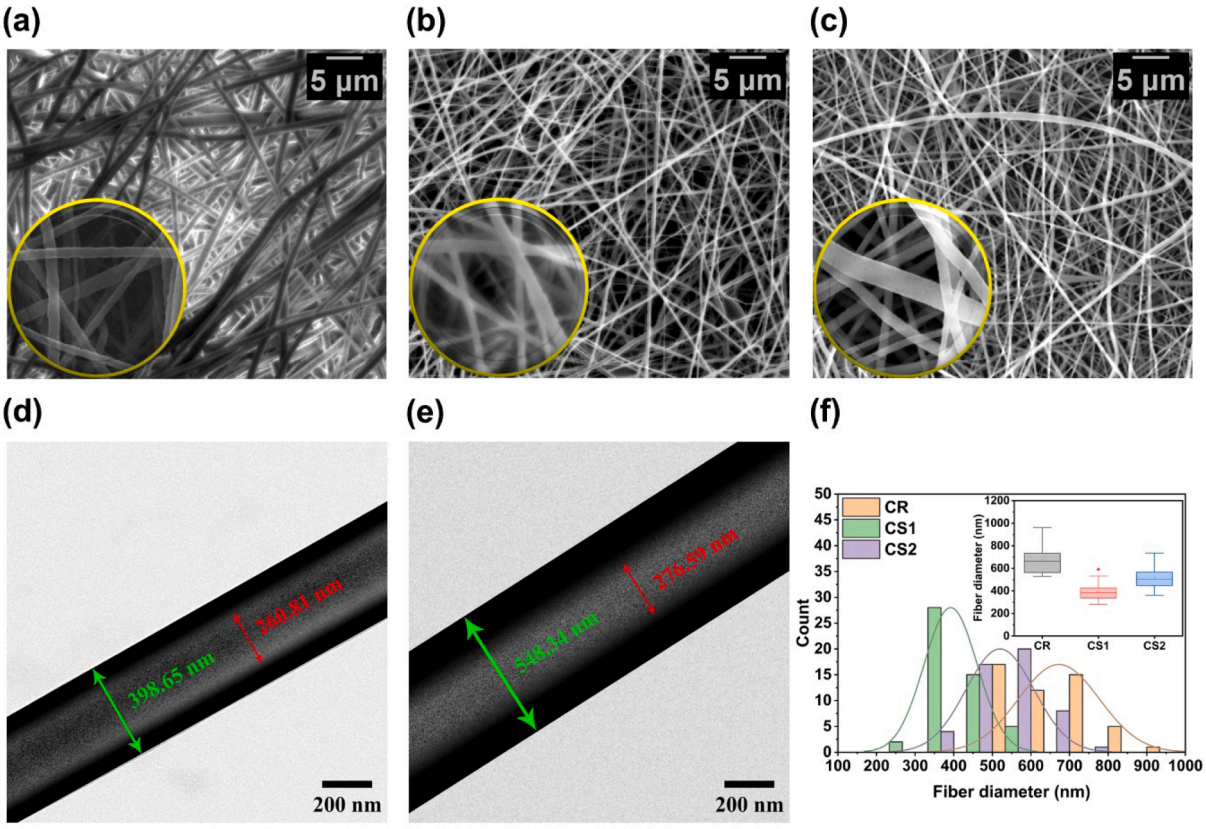

Fig. 4. SEM images of CR (a), CS1 (b), and CS2 (c) NNH meshes. TEM images of core–shell CS1 (d) and CS2 (e) NNH meshes. The diameters of the nanofibers forming each mesh group (CR, CS1, and CS2) were measured using ImageJ® software. The diameter distribution (f) analyses were done by OriginLab® software. The sample size was 100 for each group. The data were shown as mean ± SD (inset).

of alkanes), 1724 cm ^{1} (C═O stretching vibration of carbonyl groups), 1473 cm ^{1} (C—H bend of alkanes) and 1190 cm ^{1} (C—O stretching vibration of ether groups). The spectrum of amp-PCL nanofiber was similar to the spectrum of the PCL powder. The only difference was created by the —NH bend of 1° amine at 1638 cm ^{1}, indicating the amp's presence. In addition, the C═O stretching at 1726 cm ^{1} was ascribed to the non-hydrogen bonded carbonyl group (non-H-bonded C═O). Consequently, no secondary interaction-mediated compatibility (arising from hydrogen bonding) was observed between PCL and amp.

Later, the interactions between the components of NNHs were analyzed. First, the spectrum of MNP powders was investigated. A broad peak from 3620 cm ^{1} to 2660 cm ^{1} caused by the —OH and NH_2 vibrations arising from the carboxylic acid, phenolic, and aromatic amino functional groups in the indolic and pyrrolic portions of melanin (Bernsmann et al., 2010; Centeno and Shamir, 2008; Ozlu et al., 2019). Also, the bands at 2920 cm ^{1} (the stretching of —CH band), 1630 cm ^{1} (the stretching of C═O in COO^{-}, quinone, or ketone), 1453 cm ^{1} (the vibration of C═C aromatic ring vibration/the symmetric stretching of COO—) and 1388 cm ^{1} (the stretching of pyrrole ring), 1248 cm ^{1} (—CH in-plane deformation) and 1164 cm ^{1} (pyrrole —NH in-plane deformation/ring breathing) were detected. Then, the IR spectrum of the monolithic mesh (CR) was analyzed. The C═O stretching band was observed at 1725 cm ^{1}, similar to the amp-PCL spectrum. If hydrogen bonding occurs, the peak corresponding to the C═O stretching band may shift slightly to lower wavenumbers (Gurunathan et al., 2015). However, in the IR spectrum of the CR mesh, such a shift was not observed, suggesting that no hydrogen-mediated secondary interaction between MNP and amp was present. Finally, the chemical composition of core–shell hybrid mesh (CS) was analyzed to investigate the effect of core–shell formation on compatibility. No significant difference between CR and CS spectra was observed, signifying that the type of electrospinning utilized (single or coaxial nozzle) did not affect the chemical composition of the hybrid meshes or the compatibility between their forming components.

3.2.2. *Thermal analyses*

The thermal behaviors of amp and MNP powders, as well as PCL, MNPs-PCL, CR, CS1, and CS2 meshes, were investigated to evaluate the possible interaction between components influenced by the electrospinning process (Fig. S3). The amp showed three weight loss steps from 29 °C to 215 °C, 215 °C to 398 °C, and 398 °C to 556 °C, and the total weight loss was about 68 %. Since the amp is a hygroscopic compound, the first step of the thermogram could be attributed to the loss of free water and/or bound water. After bound/unbound water was evaporated, amp decomposition had been started. In the first stage, mostly non-covalent bonds were broken. However, the last stage indicated the breakage of stronger bonds, such as the covalent bonds. In the TGA curve of MNPs, two weight loss steps were identified. The first step starts at 34 °C, corresponding to the loss of bound/unbound water in MNPs, similar to the amp. Thermal decomposition began in the second step at 224 °C (Xin et al., 2015). Although the TGA was conducted until 900 °C to understand the weight loss profile of the MNPs, only 54 % of the initial mass was lost during that period (data not shown). The high thermal stability of MNPs is correlated with melanin's graphite-like structure (Dezidério et al., 2004), as confirmed by our study.

Then, the thermal stability of single-nozzle electrospun monolithic meshes, PCL, MNP-PCL, and CR was studied. According to the TGA curve of the PCL mesh, two weight loss steps between 125 °C–348 °C and 348 °C–440 °C were observed. Unlike PCL and MNPs, no weight loss up to 100 °C (corresponding to loss of free water and/or bound water) was observed due to the hydrophobic nature of the PCL. However, the presence of MNPs within the PCL matrix (MNP-PCL) caused a weight

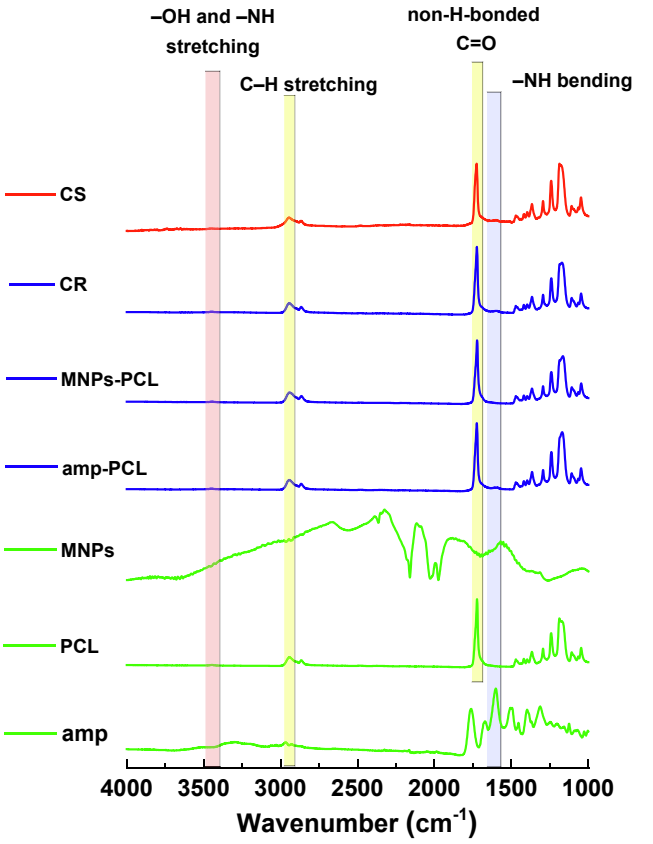

Fig. 5. ATR-FTIR spectra of the MNP, amp, and PCL powders, MNPs-PCL, amp-PCL control meshes, and NNHs (CR and CS) consisting of amp-MNPs-PCL. Green lines represent powders, blue lines show single-nozzle electrospun monolithic meshes, and the red line corresponds to coaxially electrospun core–shell fiber mesh. (For interpretation of the references to colour in this figure legend, the reader is referred to the web version of this article.)

loss starting at 209 °C. It can be due to the thermal stabilizing effect of MNPs causing a shift in the degradation temperature of the pure PCL. The CR mesh had a similar decomposition profile with two transition zones, but its degradation temperatures were decreased to 48 °C and 204 °C in the first and second zones. Although ATR-FTIR spectra did not show compatibility arising from the hydrogen bonding, the shift in the decomposition profile can be due to the electrostatic interaction (Nosanchuk et al., 2015) between amp and MNPs owing to the partially positively charged groups presence on MNPs.

Moreover, the TGA spectra of CS1 and CS2 meshes were evaluated, and two decomposition steps were monitored. The primary weight loss for CS1 and CS2 occurred at ≈200 °C, but more significant weight loss was observed in the second degradation step (≈407 °C). For the production of CS1 and CS2 meshes, identical core and shell solutions were used. Accordingly, no significant difference was found between the thermal decomposition behaviors of coaxially electrospun NNHs. Also, the decomposition profiles of CS1 and CS2 did not indicate any substantial interaction between MNPs-PCL and amp-PCL.

3.2.3. *Drug release study*

First, the characteristic absorbance peak of the free amp was determined by wavelength scanning between 1100 and 190 nm, and it was detected at 207 nm. The absorbance values were recorded for predetermined free amp concentrations (0.0025–0.02 mg/mL), and the calibration curve is sketched in Fig. S4.

The release profile of the amp from amp-PCL, CR, CS1, and CS2 meshes in PBS (pH:7.4) solution was studied for 144 h (Fig. 6). An initial burst release of the amp was observed for single-nozzle electrospun

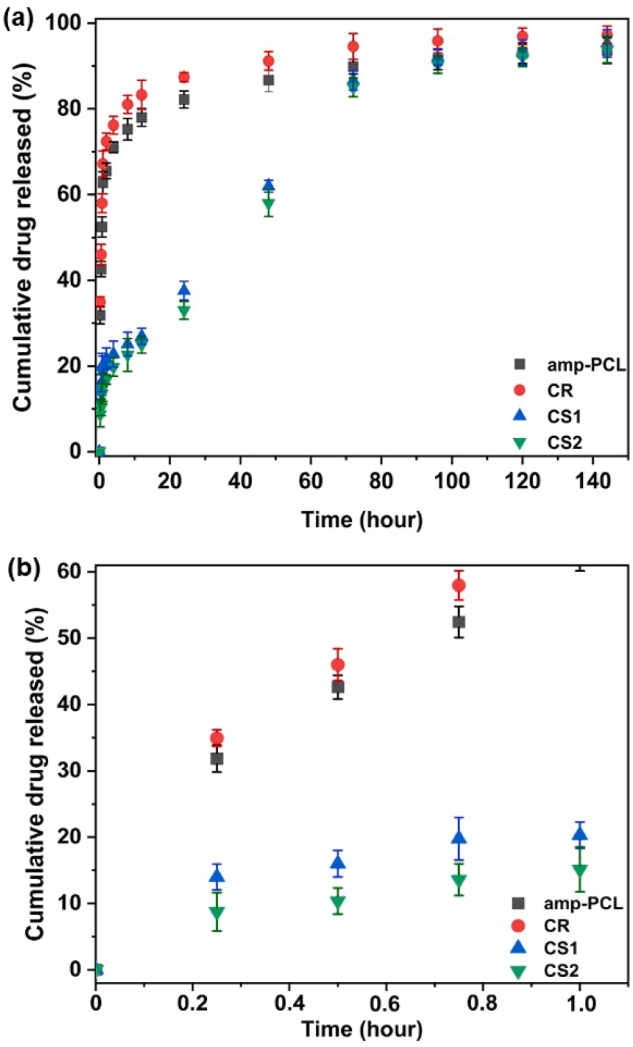

Fig. 6. In vitro drug release profiles of amp-PCL mesh, CR, CS1, and CS2 for 144 h (a) and within the first hour (b). Statistical analyses were performed with OriginLab® software using the one-way analysis of variance (one-way ANOVA) method. The data are presented as mean ± SD of triplicate measurements (n 3).

monolithic meshes: amp-PCL and CR. The remaining portions of the amp (17.15 % and 22.45 %) were released more controllably until the 72nd hour. During this period, the Korsmeyer-Peppas kinetic model was best fitted among others. The regressed equations were found as follows: $Q_{amp\text{-}PCL} = 69.183 \times t^{0.074}$ ($R^2 = 0.993$) and $Q_{CR} = 62.814 \times t^{0.082}$ ($R^2 = 0.997$), both indicating a typical Fickian diffusion-controlled release pattern (Supplementary Material, Table S2). After 72 h, the lag period began. It is noteworthy that, although the amp release trends for both meshes were found to be similar, MNPs addition, hence the hybrid formation, delayed amp release, might be owing to the electrostatic interaction formed between MNPs and amp. On the other hand, for coaxial-nozzle electrospun hybrid meshes, CS1 and CS2, the released amp ratios within the first 45 min were only 19.75 % and 13.75 %. Due to the heterogeneous distribution of the amp in nanofibers, the Peppas equation was inapplicable to characterize the release kinetics from core-shell NNHs. Because of obtaining the highest regression value (R^2), the drug release from core-shell NNHs was explained by zero-order kinetics. The regressed equations for the CS1 and CS2 hybrids between 45 min to 72 h are as follows. $Q_{CS1} = 0.926x + 18.188$ and $Q_{CS2} = 0.957x + 13.836$. The regressed equations of core–shell NNHs showed that the release rate of the amp was independent of its concentration. Only the extended diffuse layer formed by the thicker shell decreased the drug

release rate for the CS2 hybrid mesh, suggesting a more sustained behavior.

3.2.4. *In vitro evaluation of antibacterial properties*

Since ampicillin is a well-known antibiotic, its presence within the nanofibers is expected to cause bacterial inhibition. Therefore, the first series of antibacterial testing was performed by interacting MNPs and amp-free PCL, CR, CS1, and CS2 meshes with Gram-negative *E. coli* and Gram-positive *S. aureus*. At this stage, the bacteria viability was assessed by the MTT assay.

After being treated with *E. coli* for 24 h, about a 57 % increment in bacterial proliferation was observed for the PCL meshes (Fig. 7**a**). Such a boost indicates that the PCL mesh did not show any noticeable antibacterial activity; instead, high-surface-area nanofibers facilitated the adhesion and proliferation of *E. coli*. However, concerning the TCPS control, *E. coli* viability on free MNPs was decreased by 45 %. The decrement in *E. coli* viability can be explained by the considerable antibacterial activity of free MNPs (Zerrad et al., 2014). Compared to the PCL mesh, *E. coli* viabilities on CR, CS1, and CS2 meshes were decreased by 9 %, 11 %, and 8 %, respectively. Later, the antibacterial activity of the samples against *S. aureus* was studied. PCL mesh did not cause any inhibitory effect against *S. Aureus*, whereas the free MNPs repressed *S. aureus* colony formation by 52 %. After MNPs were entrapped within the NNHs, they showed no inhibitory effect against *S. aureus*. Moreover, hybrid meshes were shown their substantial antibacterial activity against the Gram-negative *E. coli* strains.

Secondly, the bacterial inhibition zone formation resulted from the interaction of single-nozzle electrospun nanofiber meshes (PCL, amp-PCL, MNPs-PCL, CR, CR-B) and core–shell hybrid meshes (CS1, CS1-B, CS2, CS2-B) with *E. coli* and *S. aureus* were evaluated (Supplementary Material, Table S1). The prior evaluation was done by testing the antibacterial activities of amp-free NNHs. It was demonstrated that CR-B, CS1-B, and CS2-B meshes had no significant effect on the inhibition of *E. coli* and *S. aureus* strains compared to the TCPS control. On the contrary, all amp-consisting meshes showed bacterial inhibition against both *E. coli* and *S. aureus*, confirming that the amp maintained its antibacterial activity although being subjected to catastrophic chemicals while solution preparation and after being exposed to high voltage throughout the electrospinning process. The drug release studies showed that monolithic NNHs released about 4-fold higher amp to the dissolution medium than the core–shell hybrids (22 % vs 80 %) in the initial period. Therefore, within the first 24 h, a more significant clear zone was expected around monolithic meshes, whereas a smaller but more controlled inhibition zone formation was presumed for core–shell meshes.

All in all, monolithic NNHs (CR) reduced the bacterial zones by about 7 % and 2 % against *E. coli* and *S. aureus*, respectively. After the same formulations were electrospun in a core–shell form, the inhibition zones of *E. coli* and *S. aureus* strains were decreased by 9 % and 5 % for CS1 meshes and 11 % and 8 % for CS2 meshes.

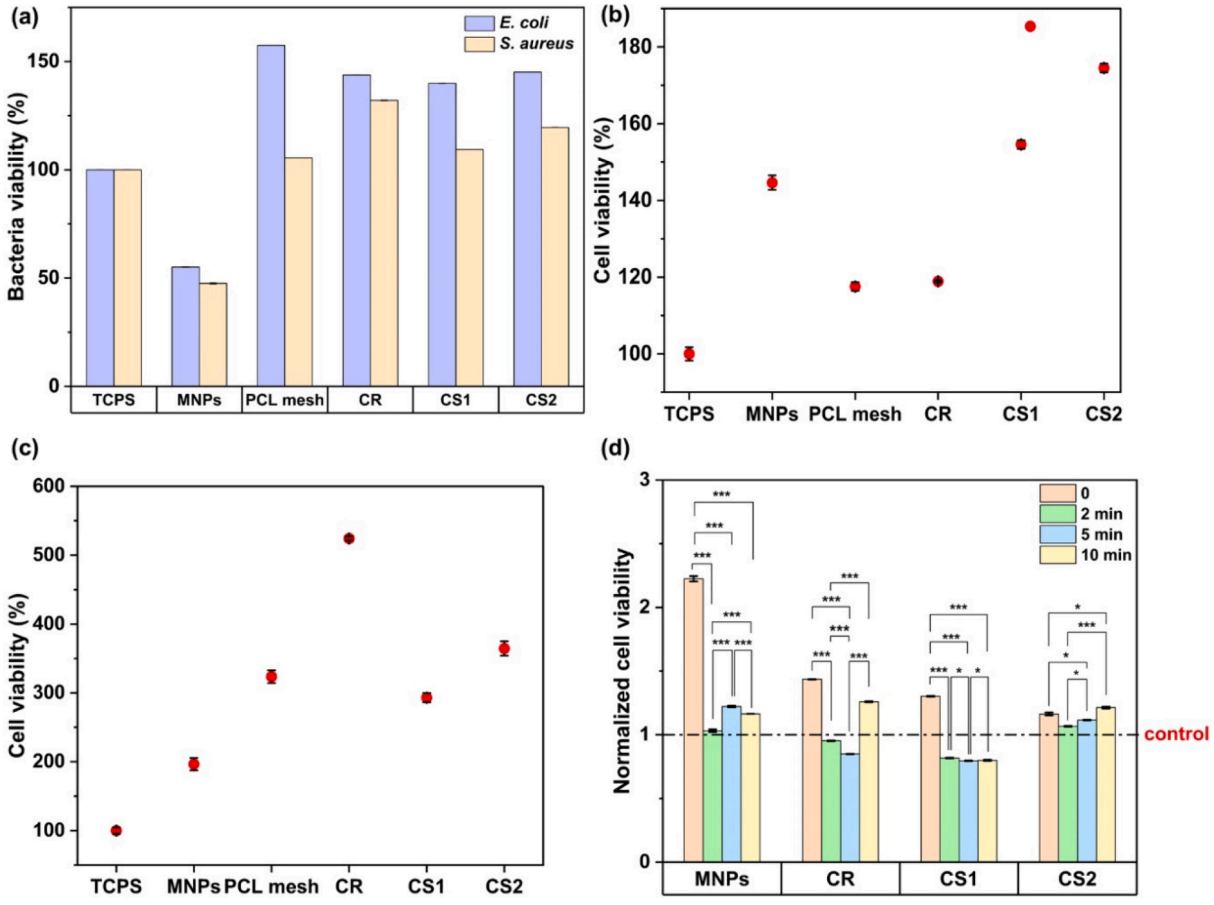

Fig. 7. (a) Antibacterial activity of MNPs and amp-free nanofiber meshes against gram-negative *E. coli* and gram-positive *S. aureus* strains. (b) In vitro fibroblast cell viabilities after the cells interacted with the MNPs and CR, CS1, and CS2. Malignant melanoma cell viabilities after introducing MNPs, and PCL, CR, CS1, and CS2 meshes (c) before UV-A exposure and (d) after UV-A light irradiation of MNPs, PCL, CR, CS1, and CS2 for different periods (0, 2, 5, and 10 min). For the evaluation of the cell viability data (a-c), TCPS (tissue culture plate surface) was taken as a negative control (NC). However, for assessing the cell viability before and after photodynamic therapy, TCPS was taken as NC for free-MNPs, whereas PCL mesh was used as NC for CR, CS1, and CS2, respectively. The data evaluation and their pairwise comparison were carried out using Tukey's honestly significant difference (HSD) method (* $p < 0.05$, *** $p < 0.001$).

3.2.5. In vitro cytotoxicity

It is essential to evaluate the cytotoxicity effect of the nanomaterials on healthy cells to estimate their potential behavior when they become in contact with a physiological environment. Therefore, we examined the cytotoxicity of the MNPs, CR, CS1, and CS2 meshes on healthy fibroblast cells. The MTT assay was performed to examine the cell viability. The results showed that free MNPs (145 %), PCL (118 %), CR (119 %), CS1 (155 %), and CS2 (175 %) meshes substantially increased fibroblast cell viabilities compared to the TCPS control (Fig. 7b). Three reasons can explain this behavior: (i) the nanoparticle's adherence to the well's surface increased the surface area, (ii) the positively charged amino groups located on the MNPs attracted negatively charged cell membrane, hence elevating cell attachment and boosted their proliferation, and (iii) 3-D structured nanofibrous meshes' mimicking ability to the native architecture of the extracellular matrix enhanced accumulation and proliferation of the cells.

3.2.6. Photodynamic therapy

The photodynamic treatment uses a light-activated drug called a photosensitizer or photosensitizing agent to kill cancer cells. Melanin is a natural photosensitizer and photoprotective nanomaterial. It can be easily activated by UV-light triggering, intercepting, and deactivating radical species within the physiological environment at specific wavelength ranges (UV-A: 315–400 nm, UV-B: 290–315 nm, and UV-C: 200–290 nm) without anti-cancer drugs. Besides, the visible range light irradiation can cause melanin to consume oxygen in the environment and release free radicals such as superoxide, hydrogen peroxide (Felix et al., 1978b), and singlet oxygen, resulting in photooxidation, which causes DNA damage (Brenner and Hearing, 2008; Takeuchi et al., 2004). Previous studies also reported that melanin forms many free radicals and reactive oxygen species (ROS) under UV-A and UV-B irradiation, indirectly damaging the DNA, proteins, and membranes or apoptosis of living cells (Akman et al., 2021; Kalyanaraman et al., 1982; Takeuchi et al., 2004). In this study, the MNPs, and amp-free CR, CS1, and CS2 meshes were evaluated to observe their lethal/photoprotective effect on metastatic melanoma cells in the absence and presence of UV-A range light stimulation.

Cell viability analyses did not reveal any lethal effect of MNPs, CR, CS1, and CS2 meshes on malignant melanoma cells before UV-A stimulus (Fig. 7**c**). In contrast, MNPs, PCL, and NNHs amplified cell adhesion and proliferation. Following the UV-A stimulus (Fig. 7**d**), the irradiation time determined the nanomaterial's tendency to cause cell death or photoprotection. For instance, MNPs exhibited photocatalyst behavior, resulting in cancer cell death by about 46 % in 2 min. After that, they started acting like photoprotective agents and resumed cell proliferation. Similarly, the NNHs showed a lethal effect on malignant melanoma cells within the first 2 min of UV-A irradiation. At this point, cell viabilities were decreased by about 34 %, 37 %, and 8 % for CR, CS1, and CS2. However, increasing the irradiation time to 5 min solely compensated for the lethal effect of UV-A owing to the photoprotection provided by the free and CS2 mesh entrapped MNPs. The protective effect of MNPs that were entrapped into CR and CS1 meshes was realized after 10 min of UV-A exposure, and under this photoprotection shield, the cancer cells continued proliferating. These results align with our previous finding, which demonstrated that the UV-A (at 1 cm distance) irradiated MNPs (100 μg/mL) generated singlet oxygen species only within 1 min (Akman et al., 2021).

The comparable photocatalytic activity of CR and CS1 meshes can be explained by the similar amount of ROS generated by both meshes. In detail, although the CR mesh comprised almost doubled MNPs than the CS1 mesh, MNPs in the CR matrix were homogenously distributed in a higher volume (nanofiber diameter ~ 672 nm). Only the MNPs closer to the surface could transmit the generated ROS to the fiber's surface, which inhibits melanoma cells. Besides, CS1 and CS2 captured similar amounts of MNPs within their shells. Nevertheless, due to the CS1 shell thickness being much smaller than the CS2 (69 nm vs 136 nm), the more effortless transfer of ROS from the CS1 mesh yielded much higher cell inhibition in a shorter time.

4. Conclusion and perspectives

Melanin is an abundant pigment found in most living organisms and is a promising sustainable material that can be utilized to boost several fields ranging from electronics to bioapplications. Although its unique physicochemical nature promises several functionalities, such as (i) biocompatibility and biodegradability, (ii) high stability, (iii) stimuli-responsiveness, (iv) metal chelation, (v) photocatalytic and paramagnetic properties, (vi) radioprotection due to the ability to absorb UV and visible radiation, its application as NNHs has not been explored.

We provide a versatile electrospinning strategy to produce MNP-enhanced PCL hybrid nanocomposites to fill this particular gap. Although the building components of NNHs had low compatibility with each other (shown in the thermal analysis), the morphological examination proved the suitability of the electrospinning method to form hybrid meshes in a single step. The drug delivery and photodynamic therapy capabilities of the multifunctional NNHs were demonstrated for the proof of concept. The release studies showed that the drug transport from hybrid meshes followed either Fickian transport or zero-order kinetics for monolithic and core–shell hybrids. The existence of MNPs in the monolithic meshes lowered the burst release of the amp than its conventional free dosage form (Nairi et al., 2017) and the amp-PCL mesh (Sultanova et al., 2016). Also, previously reported non-Fickian transport of drugs from MNPs (Araújo et al., 2014) could have been improved by MNPs. Modulating the drug release employed by such a simple approach can eliminate the disadvantages of the disease-site targeted burst release approach that systemic drug delivery systems rely on.

In addition to its proven biocompatibility and antibacterial features, the photosynthesizer MNPs entrapped within the NNHs decreased metastatic melanoma cell viabilities by 34 % for monolithic NNHs, 37 % for CS1 and 8 % for CS2 (in comparison to non-UV-A treated surfaces) after 2 min of UV-A irradiation. Since NNHs demonstrated success in drug delivery and photodynamic therapy, we can state that the electrospinning produced NNHs-based transdermal patches can facilitate malignant melanoma treatment. The infrared-range stimulus for on-demand deep tissue photodynamic therapy is currently under investigation to facilitate post-operation treatment of other cancer types.

CRediT authorship contribution statement

Gözde Kabay: Conceptualization, Methodology, Formal analysis, Visualization, Investigation, Supervision, Data curation, Writing – original draft, Writing – review & editing. **Ahmet Ersin Meydan:** Conceptualization, Methodology, Investigation. **Taesik Eom:** Investigation. **Gizem Kaleli-Can:** Supervision, Formal analysis, Investigation, Writing – review & editing.

Declaration of Competing Interest

The authors declare that they have no known competing financial interests or personal relationships that could have appeared to influence the work reported in this paper.

Data availability

Data will be made available on request.

Acknowledgments

BSS acknowledges the funding support from NRF-2021R1A4A1022920 and NRF-2020R1F1A1075944.

Notes

We dedicate this article to the memory of our academic father, Prof. Mehmet Mutlu. “Old chemists never die; they just reach equilibrium.’’

Appendix A. Supplementary data

Supplementary data to this article can be found online at https://doi.org/10.1016/j.ijpharm.2022.122442.

References

Adhikari, U., An, X., Rijal, N., Hopkins, T., Khanal, S., Chavez, T., Tatu, R., Sankar, J., Little, K.J., Hom, D.B., Bhattarai, N., Pixley, S.K., 2019. Embedding magnesium metallic particles in polycaprolactone nanofiber mesh improves applicability for biomedical applications. Acta Biomater. 98, 215–234. https://doi.org/10.1016/j.actbio.2019.04.061.

Ajdary, M., Moosavi, M., Rahmati, M., Falahati, M., Mahboubi, M., Mandegary, A., Jangjoo, S., Mohammadinejad, R., Varma, R., 2018. Health concerns of various nanoparticles: a review of their in vitro and in vivo toxicity. Nanomaterials 8 (9), 634.

Akman, B., İslam, B., Kaleli-Can, G., Topaloğlu, N., Karaman, D.Ş., Baysoy, E., 2021. Gıda ve Sağlık Uygulamaları İçin UV-A Işıma Altında Alternatif Bir Fotokatalizör Olarak Doğal Melanin Nanoparçacıkları. Avrupa Bilim ve Teknoloji Dergisi 32, 940–946. https://doi.org/10.31590/EJOSAT.1040830.

Anand, P., Stahel, V.P., 2021. The safety of Covid-19 mRNA vaccines: a review. Patient Saf. Surg. 15, 20. https://doi.org/10.1186/s13037-021-00291-9.

Araújo, M., Viveiros, R., Correia, T.R., Correia, I.J., Bonifácio, V.D.B., Casimiro, T., Aguiar-Ricardo, A., 2014. Natural melanin: A potential pH-responsive drug release device. Int. J. Pharm. 469, 140–145. https://doi.org/10.1016/j.ijpharm.2014.04.051.

Baden, L.R., el Sahly, H.M., Essink, B., Kotloff, K., Frey, S., Novak, R., Diemert, D., Spector, S.A., Rouphael, N., Creech, C.B., McGettigan, J., Khetan, S., Segall, N., Solis, J., Brosz, A., Fierro, C., Schwartz, H., Neuzil, K., Corey, L., Gilbert, P., Janes, H., Follmann, D., Marovich, M., Mascola, J., Polakowski, L., Ledgerwood, J., Graham, B.S., Bennett, H., Pajon, R., Knightly, C., Leav, B., Deng, W., Zhou, H., Han, S., Ivarsson, M., Miller, J., Zaks, T., 2021. Efficacy and Safety of the mRNA-1273 SARS-CoV-2 Vaccine. N. Engl. J. Med. 384, 403–416. https://doi.org/10.1056/NEJMoa2035389.

Banerjee, A., Jariwala, T., Baek, Y.-K., To, D.T.H., Tai, Y., Liu, J., Park, H., Myung, N. v, Nam, J., 2021. Magneto- and opto-stimuli responsive nanofibers as a controlled drug delivery system. Nanotechnology 32, 505101. https://doi.org/10.1088/1361-6528/ac2700.

Bernsmann, F., Ersen, O., Voegel, J.-C., Jan, E., Kotov, N.A., Ball, V., 2010. Melanin-Containing Films: Growth from Dopamine Solutions versus Layer-by-Layer Deposition. ChemPhysChem 11, 3299–3305. https://doi.org/10.1002/cphc.201000384.

Bohara, R.A., 2019. Introduction and Types of Hybrid Nanostructures for Medical Applications, in: Hybrid Nanostructures for Cancer Theranostics. Elsevier, pp. 1–16. https://doi.org/10.1016/B978-0-12-813906-6.00001-9.

Brenner, M., Hearing, V.J., 2008. The Protective Role of Melanin Against UV Damage in Human Skin†. Photochem. Photobiol. 84, 539–549. https://doi.org/10.1111/J.1751-1097.2007.00226.X.

Bryaskova, R., Pencheva, D., Kale, G.M., Lad, U., Kantardjiev, T., 2010. Synthesis, characterisation and antibacterial activity of PVA/TEOS/Ag-Np hybrid thin films. J. Colloid Interface Sci. 349, 77–85. https://doi.org/10.1016/j.jcis.2010.04.091.

Buschmann, M.D., Carrasco, M.J., Alishetty, S., Paige, M., Alameh, M.G., Weissman, D., 2021. Nanomaterial Delivery Systems for mRNA Vaccines. Vaccines (Basel) 9, 65. https://doi.org/10.3390/vaccines9010065.

Centeno, S.A., Shamir, J., 2008. Surface enhanced Raman scattering (SERS) and FTIR characterization of the sepia melanin pigment used in works of art. J. Mol. Struct. 873, 149–159. https://doi.org/10.1016/j.molstruc.2007.03.026.

Chiarelli-Neto, O., Ferreira, A.S., Martins, W.K., Pavani, C., Severino, D., Faião-Flores, F., Maria-Engler, S.S., Aliprandini, E., Martinez, G.R., Di Mascio, P., Medeiros, M.H.G., Baptista, M.S., Battista, J.R., 2014. Melanin Photosensitization and the Effect of Visible Light on Epithelial Cells. PLoS One 9 (11), e113266.

Clasky, A.J., Watchorn, J.D., Chen, P.Z., Gu, F.X., 2021. From prevention to diagnosis and treatment: Biomedical applications of metal nanoparticle-hydrogel composites. Acta Biomater. 122, 1–25. https://doi.org/10.1016/j.actbio.2020.12.030.

Deng, X., Zhao, Y., Gao, H., Wang, D., Miao, Z., Cao, H., Yang, Z., He, W., 2021. Studies on electro-optical properties of polymer dispersed liquid crystals doped with reticular nanofiber films prepared by electrospinning. Liq. Cryst. 48, 1850–1858. https://doi.org/10.1080/02678292.2021.1902583.

Dezidério, S.N., Brunello, C.A., da Silva, M.I.N., Cotta, M.A., Graeff, C.F.O., 2004. Thin films of synthetic melanin. J. Non Cryst. Solids 338–340, 634–638. https://doi.org/10.1016/j.jnoncrysol.2004.03.058.

Dong, R., Guo, B., 2021. Smart wound dressings for wound healing. Nano Today 41, 101290. https://doi.org/10.1016/j.nantod.2021.101290.

Endres, H.J., Siebert-Raths, A., 2012. Performance Profile of Biopolymers Compared to Conventional Plastics. Polymer Science: A Comprehensive Reference, 10 Volume Set 10, 317–353. https://doi.org/10.1016/B978-0-444-53349-4.00270-3.

Eom, T., Woo, K., Shim, B.S., 2016. Melanin: a naturally existing multifunctional material. Appl. Chem. Eng. 27, 115–122. https://doi.org/10.14478/ace.2016.1029.

Eom, T., Woo, K., Cho, W., Heo, J.E., Jang, D., Shin, J.I., Martin, D.C., Wie, J.J., Shim, B.S., 2017. Nanoarchitecturing of natural melanin nanospheres by layer-by-layer assembly: macroscale anti-inflammatory conductive coatings with optoelectronic tunability. Biomacromolecules 18, 1908–1917. https://doi.org/10.1021/acs.biomac.7b00336.

Eom, T., Jeon, J., Lee, S., Woo, K., Heo, J.E., Martin, D.C., Wie, J.J., Shim, B.S., 2019. Naturally derived melanin nanoparticle composites with high electrical conductivity and biodegradability. Part. Part. Syst. Char. 36, 1900166. https://doi.org/10.1002/PPSC.201900166.

Felix, C.C., Hyde, J.S., Sarna, T., Sealy, R.C., 1978a. Interactions of melanin with metal ions. Electron spin resonance evidence for chelate complexes of metal ions with free radicals. J. Am. Chem. Soc. 100, 3922–3926. https://doi.org/10.1021/ja00480a044.

Felix, C.C., Hyde, J.S., Sarna, T., Sealy, R.C., 1978b. Melanin photoreactions in aerated media: Electron spin resonance evidence for production of superoxide and hydrogen peroxide. Biochem. Biophys. Res. Commun. 84, 335–341. https://doi.org/10.1016/0006-291X(78)90175-4.

Feynman, R.P., 1992. There’s plenty of room at the bottom. J. Microelectromech. Syst. 1, 60–66. https://doi.org/10.1109/84.128057.

Gabriele, V.R., Mazhabi, R.M., Alexander, N., Mukherjee, P., Seyfried, T.N., Nwaji, N., Akinoglu, E.M., Mackiewicz, A., Zhou, G., Giersig, M., Naughton, M.J., Kempa, K., 2021. Light- and Melanin Nanoparticle-Induced Cytotoxicity in Metastatic Cancer Cells. Pharmaceutics 2021, Vol. 13, Page 965 13, 965. https://doi.org/10.3390/PHARMACEUTICS13070965.

Gurunathan, T., Mohanty, S., Nayak, S.K., 2015. Effect of reactive organoclay on physicochemical properties of vegetable oil-based waterborne polyurethane nanocomposites. RSC Adv. 5, 11524–11533. https://doi.org/10.1039/C4RA14601H.

Jeevanandam, J., Barhoum, A., Chan, Y.S., Dufresne, A., Danquah, M.K., 2018. Review on nanoparticles and nanostructured materials: history, sources, toxicity and regulations. Beilstein J. Nanotechnol. 9, 1050–1074. https://doi.org/10.3762/bjnano.9.98.

Ji, X., Li, R., Liu, G., Jia, W., Sun, M., Liu, Y., Luo, Y., Cheng, Z., 2021. Phase separation-based electrospun Janus nanofibers loaded with Rana chensinensis skin peptides/silver nanoparticles for wound healing. Mater. Des. 207, 109864 https://doi.org/10.1016/j.matdes.2021.109864.

Kabay, G., Meydan, A.E.A.E., Can, G.K., Demirci, C., Mutlu, M., Kaleli Can, G., Demirci, C., Mutlu, M., 2017. Controlled release of a hydrophilic drug from electrospun amyloid-like protein blend nanofibers. Mater. Sci. Eng. C 81, 271–279. https://doi.org/10.1016/j.msec.2017.08.003.

Kabay, G., Demirci, C., Kaleli Can, G., Meydan, A.E., Daşan, B.G., Mutlu, M., 2018. A comparative study of single-needle and coaxial electrospun amyloid-like protein nanofibers to investigate hydrophilic drug release behavior. Int. J. Biol. Macromol. 114, 989–997.

Kabay, G., Manz, A., Dincer, C., Kabay, G., Dincer, C., Manz, A., 2022. Microfluidic Roadmap for Translational Nanotheranostics. Small Methods 6, 2101217. https://doi.org/10.1002/SMTD.202101217.

Kaleli-Can, G., Ozlu, B., Özgüzar, H.F., Onal-Ulusoy, B., Kabay, G., Eom, T., Shim, B.S., Mutlu, M., 2020. Natural Melanin Nanoparticle-decorated Screen-printed Carbon Electrode: Performance Test for Amperometric Determination of Hexavalent Chromium as Model Trace. Electroanalysis 32, 1696–1706. https://doi.org/10.1002/elan.202000038.

Kalyanaraman, B., Felix, C.C., Sealy, R.C., 1982. Photoionization of Melanin Precursors: An Electron Spin Resonance Investigation Using The Spin Trap 5,5-Dimethyl-1-Pyrroline-1-Oxide (DMPO). Photochem. Photobiol. 36, 5–12. https://doi.org/10.1111/J.1751-1097.1982.TB04332.X.

Katz, E., Willner, I., 2004. Integrated Nanoparticle-Biomolecule Hybrid Systems: Synthesis, Properties, and Applications. Angew. Chem. Int. Ed. 43, 6042–6108. https://doi.org/10.1002/anie.200400651.

Liu, L., Hu, S., Gao, K., 2020. Cellulose nanofiber based flexible N-doped carbon mesh for energy storage electrode with super folding endurance. Mater. Today Energy 17, 100441.

Liu, Y., Simon, J.D., 2003. Isolation and biophysical studies of natural eumelanins: applications of imaging technologies and ultrafast spectroscopy. Pigment Cell Res. 16, 606–618. https://doi.org/10.1046/J.1600-0749.2003.00098.X.

Loh, X.J., Peh, P., Liao, S., Sng, C., Li, J., 2010. Controlled drug release from biodegradable thermoresponsive physical hydrogel nanofibers. J. Control. Release 143, 175–182. https://doi.org/10.1016/j.jconrel.2009.12.030.

Ma, K., Liao, C., Huang, L., Liang, R., Zhao, J., Zheng, L., Su, W., 2021. Electrospun PCL/MoS 2 Nanofiber Membranes Combined with NIR-Triggered Photothermal Therapy to Accelerate Bone Regeneration. Small 17, 2104747. https://doi.org/10.1002/smll.202104747.

Mavridi-Printezi, A., Guernelli, M., Menichetti, A., Montalti, M., 2020. Bio-Applications of Multifunctional Melanin Nanoparticles: From Nanomedicine to Nanocosmetics. Nanomaterials 2020, Vol. 10, Page 2276 10, 2276. https://doi.org/10.3390/NANO10112276.

Morsink, M., Severino, P., Luna-Ceron, E., Hussain, M.A., Sobahi, N., Shin, S.R., 2022. Effects of electrically conductive nano-biomaterials on regulating cardiomyocyte behavior for cardiac repair and regeneration. Acta Biomater. 139, 141–156. https://doi.org/10.1016/j.actbio.2021.11.022.

Nairi, V., Medda, L., Monduzzi, M., Salis, A., 2017. Adsorption and release of ampicillin antibiotic from ordered mesoporous silica. J. Colloid Interface Sci. 497, 217–225. https://doi.org/10.1016/J.JCIS.2017.03.021.

Nakielski, P., Pawłowska, S., Rinoldi, C., Ziai, Y., de Sio, L., Urbanek, O., Zembrzycki, K., Pruchniewski, M., Lanzi, M., Salatelli, E., Calogero, A., Kowalewski, T.A., Yarin, A.L.,

Pierini, F., 2020. Multifunctional Platform Based on Electrospun Nanofibers and Plasmonic Hydrogel: A Smart Nanostructured Pillow for Near-Infrared Light-Driven Biomedical Applications. ACS Appl. Mater. Interfaces 12, 54328–54342. https://doi.org/10.1021/acsami.0c13266.

Nosanchuk, J.D., Stark, R.E., Casadevall, A., 2015. Fungal Melanin: What do We Know About Structure? Front. Microbiol. 6 https://doi.org/10.3389/fmicb.2015.01463.

Ozlu, B., Kabay, G., Bocek, I., Yilmaz, M., Piskin, A.K., Shim, B.S., Mutlu, M., 2019. Controlled release of doxorubicin from polyethylene glycol functionalized melanin nanoparticles for breast cancer therapy: Part I. Production and drug release performance of the melanin nanoparticles. Int. J. Pharm. 570, 118613.

Pan, Z., Zhai, J., Shen, B., 2017. Multilayer hierarchical interfaces with high energy density in polymer nanocomposites composed of BaTiO 3 @TiO 2 @Al 2 O 3 nanofibers. J. Mater. Chem. A Mater. 5, 15217–15226. https://doi.org/10.1039/C7TA03846A.

Polack, F.P., Thomas, S.J., Kitchin, N., Absalon, J., Gurtman, A., Lockhart, S., Perez, J.L., Pérez Marc, G., Moreira, E.D., Zerbini, C., Bailey, R., Swanson, K.A., Roychoudhury, S., Koury, K., Li, P., Kalina, W.V., Cooper, D., Frenck, R.W., Hammitt, L.L., Türeci, Ö., Nell, H., Schaefer, A., Ünal, S., Tresnan, D.B., Mather, S., Dormitzer, P.R., Şahin, U., Jansen, K.U., Gruber, W.C., 2020. Safety and Efficacy of the BNT162b2 mRNA Covid-19 Vaccine. N. Engl. J. Med. 383 (27), 2603–2615.

Qiao, Z., Shen, M., Xiao, Y., Zhu, M., Mignani, S., Majoral, J.-P., Shi, X., 2018. Organic/inorganic nanohybrids formed using electrospun polymer nanofibers as nanoreactors. Coord. Chem. Rev. 372, 31–51. https://doi.org/10.1016/j.ccr.2018.06.001.

Różanowska, M., Sarna, T., Land, E.J., Truscott, T.G., 1999. Free radical scavenging properties of melanin. Interaction of eu and pheo melanin models with reducing and oxidizing agents. Free Radic. Biol. Med. 26 (5-6), 518–525.

Sahin, U., Muik, A., Vogler, I., Derhovanessian, E., Kranz, L.M., Vormehr, M., Quandt, J., Bidmon, N., Ulges, A., Baum, A., Pascal, K.E., Maurus, D., Brachtendorf, S., Lörks, V., Sikorski, J., Koch, P., Hilker, R., Becker, D., Eller, A.-K., Grützner, J., Tonigold, M., Boesler, C., Rosenbaum, C., Heesen, L., Kühnle, M.-C., Poran, A., Dong, J.Z., Luxemburger, U., Kemmer-Brück, A., Langer, D., Bexon, M., Bolte, S., Palanche, T., Schultz, A., Baumann, S., Mahiny, A.J., Boros, G., Reinholz, J., Szabó, G.T., Karikó, K., Shi, P.-Y., Fontes-Garfias, C., Perez, J.L., Cutler, M., Cooper, D., Kyratsous, C.A., Dormitzer, P.R., Jansen, K.U., Türeci, Ö., 2021. BNT162b2 vaccine induces neutralizing antibodies and poly-specific T cells in humans. Nature 595, 572–577. https://doi.org/10.1038/s41586-021-03653-6.

Schoenmaker, L., Witzigmann, D., Kulkarni, J.A., Verbeke, R., Kersten, G., Jiskoot, W., Crommelin, D.J.A., 2021. mRNA-lipid nanoparticle COVID-19 vaccines: Structure and stability. Int. J. Pharm. 601, 120586 https://doi.org/10.1016/j.ijpharm.2021.120586.

Sultanova, Z., Kaleli, G., Kabay, G., Mutlu, M., 2016. Controlled release of a hydrophilic drug from coaxially electrospun polycaprolactone nanofibers. Int. J. Pharm. 505, 133–138. https://doi.org/10.1016/j.ijpharm.2016.03.032.

Takeuchi, S., Zhang, W., Wakamatsu, K., Ito, S., Hearing, V.J., Kraemer, K.H., Brash, D.E., 2004. Melanin acts as a potent UVB photosensitizer to cause an atypical mode of cell death in murine skin. PNAS 101, 15076–15081. https://doi.org/10.1073/PNAS.0403994101/ASSET/D8C5F320-F417-40AF-89DE-2A2B762AA268/ASSETS/GRAPHIC/ZPQ0430462700005.JPEG.

Tang, J., Yin, Q., Shi, M., Yang, M., Yang, H., Sun, B., Guo, B., Wang, T., 2021. Programmable shape transformation of 3D printed magnetic hydrogel composite for hyperthermia cancer therapy. Extreme Mech. Lett. 46, 101305 https://doi.org/10.1016/j.eml.2021.101305.

Taylor-Pashow, K.M.L., Della Rocca, J., Huxford, R.C., Lin, W., 2010. Hybrid nanomaterials for biomedical applications. Chem. Commun. 46 (32), 5832.

Wang, Y., Wang, B., Qiao, W., Yin, T., 2010. A Novel Controlled Release Drug Delivery System for Multiple Drugs Based on Electrospun Nanofibers Containing Nanoparticles. J. Pharm. Sci. 99, 4805–4811. https://doi.org/10.1002/jps.22189.

Wang, S., Zhao, Y., Shen, M., Shi, X., 2012. Electrospun hybrid nanofibers doped with nanoparticles or nanotubes for biomedical applications. Ther. Deliv. 3, 1155–1169. https://doi.org/10.4155/tde.12.103.

Xiao, M., Shawkey, M.D., Dhinojwala, A., 2020. Bioinspired Melanin-Based Optically Active Materials. Adv. Opt. Mater. 8, 2000932. https://doi.org/10.1002/adom.202000932.

Xie, J., Li, H., Che, H., Dong, X., Yang, X., Xie, W., 2021. Extraction, physicochemical characterisation, and bioactive properties of ink melanin from cuttlefish (Sepia esculenta). Int. J. Food Sci. Technol. 56, 3627–3640. https://doi.org/10.1111/IJFS.14992.

Xin, C., Ma, J., Tan, C., Yang, Z., Ye, F., Long, C., Ye, S., Hou, D., 2015. Preparation of melanin from Catharsius molossus L. and preliminary study on its chemical structure. J. Biosci. Bioeng. 119, 446–454. https://doi.org/10.1016/j.jbiosc.2014.09.009.

Zerrad, A., Anissi, J., Ghanam, J., Sendide, K., el Hassouni, M., 2014. Antioxidant and antimicrobial activities of melanin produced by a Pseudomonas Balearica strain. J. Biotechnol. Lett. 5, 87–93.

Zhang, R., Fan, Q., Yang, M., Cheng, K., Lu, X., Zhang, L., Huang, W., Cheng, Z., 2015. Engineering Melanin Nanoparticles as an Efficient Drug-Delivery System for Imaging-Guided Chemotherapy. Adv. Mater. 27, 5063–5069. https://doi.org/10.1002/ADMA.201502201.

Zhang, M., Song, W., Tang, Y., Xu, X., Huang, Y., Yu, D., 2022. Polymer-Based Nanofiber-Nanoparticle Hybrids and Their Medical Applications. Polymers (Basel) 14, 351. https://doi.org/10.3390/polym14020351.

Zhao, R., Zhang, X., Peng, S., Hong, P., Zou, T., Wang, Z., Xing, X., Yang, Y., Wang, Y., 2020. Shaddock peels as bio-templates synthesis of Cd-doped SnO2 nanofibers: A high performance formaldehyde sensing material. J. Alloy. Compd. 813, 152170 https://doi.org/10.1016/j.jallcom.2019.152170.